applied sciences

MDPI

Article

Selective Alkali Activation of Limestone for Additive Manufacturing in Construction: Influence of Alkali Concentration on Physical and Mechanical Properties

Mursaleen Shahid [1,*], Alexandre Pierre [2], Annelise Cousture [2] and Vincenzo M. Sglavo [1]

[1] Department of Industrial Engineering, University of Trento, 38123 Trento, Italy
[2] Laboratoire de Mécanique et Matériaux du Génie Civil, CY Cergy Paris Université, F-95000 Cergy, France
* Correspondence: mursaleen.shahid@unitn.it

Featured Application: Additive Manufacturing for Novel and Advanced Materials: Characteristics, Challenges, and Applications.

Abstract: Alkali-activated binders are gaining importance in the construction industry because of their environmental and mechanical advantages. This paper focuses on selective limestone activation (SLA) using aqueous sodium hydroxide solutions to be used as a non-hydraulic binder material. This study investigates the mechanical performance of 3D-printed specimens cured at 45 °C produced with different NaOH concentrations. Varying the NaOH concentration is significant for analyzing its role in optimizing the reactivity and mechanical behavior for additive manufacturing applications. The results show that mechanical strength and physical properties are influenced by the NaOH concentration, with the strength decreasing at higher sodium hydroxide loads. Although porosity and density are consistent in all concentrations, microstructure examination showed non-homogeneous grainy texture.

Keywords: 3D printing; limestone; mechanical properties; selective limestone activation; NaOH concentrations

check for updates

Academic Editors: Edgar Moraru and Manoj Gupta

Received: 7 March 2025
Revised: 15 April 2025
Accepted: 16 April 2025
Published: 17 April 2025

Citation: Shahid, M.; Pierre, A.; Cousture, A.; Sglavo, V.M. Selective Alkali Activation of Limestone for Additive Manufacturing in Construction: Influence of Alkali Concentration on Physical and Mechanical Properties. *Appl. Sci.* **2025**, *15*, 4453. https://doi.org/10.3390/app15084453

1. Introduction

The construction industry is a major contributor to the global economy, but it has been mainly relying on traditional technologies, although the trend is changing after the digitalization in industry after the 1970s. Based on this, additive manufacturing (AM) has achieved significant progress in the construction industry, bringing innovative approaches to the design and production of building elements. AM is a process to fabricate physical objects directly from computer-aided design models in a layer-by-layer manner [1–4]. Among the different additive manufacturing techniques that can be used in construction, as shown in Figure 1, selective cement activation is a process of interest in the field of selective particles bed binding.

The "selective particles bed binding" technique can be divided into two methods [5]. In the so-called "selective paste intrusion", a component is fabricated by spreading thin layers of aggregate, followed by the local application of cement paste to achieve hardening [6]. The second method, "selective cement activation (SCA)", relates to local hardening obtained by spraying water on a layer of mixed cement and aggregate [7–10]. This process is composed of two main steps. In the first one, the dry powder is uniformly distributed as a thin layer with the aid of a roller or doctor blade of the required layer thickness. The second step involves the activation of the powder by the liquid phase sprayed through a travelling nozzle. The technique when used for the activation of limestone is called selective limestone activation (SLA).

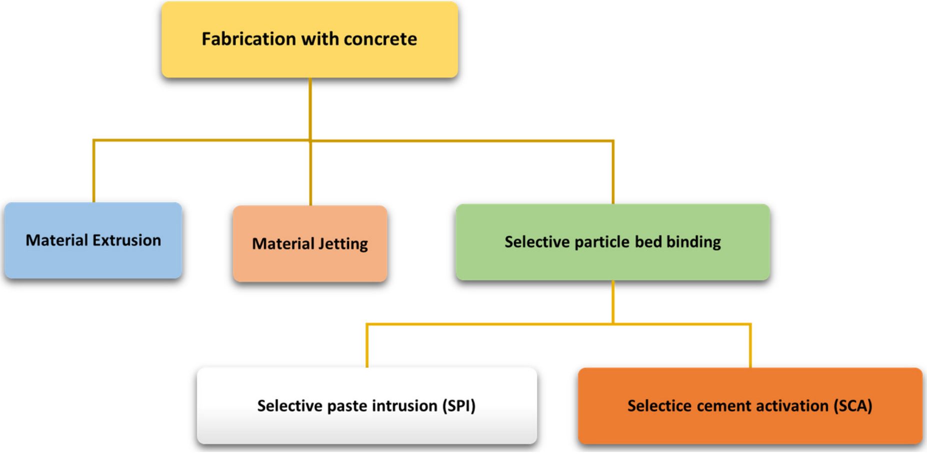

Figure 1. Additive manufacturing processes for concrete fabrication.

Lowke et al. [11] examined the use of water in selective cement activation in two configurations: (a) spraying very small droplets (in the picoliter range) onto the particle bed or (b) jetting water at variable pressure. The strength achieved without post-treatment reaches 15.5 MPa, which classifies the material as lightweight concrete with a bulk density of 1.6 g/cm^3. The authors did observe that higher water-to-cement ratios decrease porosity and increase strength, but reduce shape accuracy. Similarly, larger aggregate particle sizes produced superior strengths with loss of shape accuracy, while higher water jet pressure had insignificant effects on strengths and shape accuracy, but increased porosity and reduced homogeneity. Lowke et al. [12] extended the original model based on the Washburn equation for the time-dependent prediction of fluid intrusion into particle beds. Their study indicated that the initial fluid penetration (capillary intrusion) is very rapid and almost spontaneous with no significant influence from the particle size, followed by further capillary action, which is responsible for inter-layer bonding and geometric precision.

Shahid et al. [13] focused on the behavior of a blended binary cement mixture, consisting of ordinary Portland cement (OPC) and quick-setting cement in binder jetting 3D printing. It was observed that OPC content in the dry mixtures affected the flow properties, with a lower OPC concentration showing better flowability. A higher OPC content enhanced the density of the 3D-printed specimens, together with the mechanical properties. Salari et al. [14] used magnesium oxychloride cement-based material and investigated the interaction of the powder and binder to point out how the binder droplets interact with the powder bed to affect the quality of the printed blocks. The mechanical strength was generally correlated with the volume of cementitious bonds; finer particles provided a larger surface area for bonding, thereby improving the resistance. In another work, Ur Rahman et al. [15] focused on the 3D printing of geopolymer-based concrete: metakaolin was selectively activated using an alkaline activated solution and the maximum modulus of rupture obtained was 4.4 MPa.

Despite the growing interest in materials obtained by alkali activation, very little research has been focused on the alkali activation of calcium-carbonate-containing compounds like, for example, limestone. It was through a patent published in 2006 that early investigations into the use of limestone as a precursor, activated by sodium hydroxide without the addition of silicate phases, were initiated [16]. Studies concerned with recent cement production have increasingly focused on its minimal environmental impact. Limestone offers considerable advantages due to its structural purity, availability, and cost-effectiveness compared with conventional cement. Many researchers have explored its potential to act as a substitute for cement for this reason. An inceptive study considered aspects such as CO_2 emissions, temperature effects, workability, density, shrinkage, compressive strength, mortar strength, and porosity [17]. From the results, it was concluded that higher percentages of limestone contributed largely to CO_2 emission reductions, and with a 10% increase in limestone powder, the percentage reduction in emission was about 8–9%. It was also found that the replacement strengthened the distribution and workability while reducing the porosity and shrinkage, the compressive strength anyway decreasing. In addition, for mortar and concrete, the limestone particle size had a minor effect on all the levels of replacement. Nevertheless, studies on the development of alkali activation of calcium carbonate are few [18–20] and have mainly focused on conventional casting methods. However, their applications in 3D printing remain largely unexplored.

The present study investigates the properties of 3D-printed limestone material activated with different NaOH water solutions. The phase stability, mineral composition, and mechanical properties were studied. The results obtained from this work allow for a better understanding of the influence of NaOH concentration on properties that make printed limestone materials suitable for applications in the construction industry.

2. Materials and Methods

A customized 3D printer was utilized for the dry powder supply and liquid binder supply, as shown in Figure 2. A positive displacement metering valve MV 250 (Poly Dispensing Systems, Orgeval, France) was integrated into the printer to ensure accurate binder deposition using a 700 ETC+ controller (Poly Dispensing Systems, Orgeval, France), thus enhancing the precision of the specimen's fabrication. The hopper was used for the dry powder supply while the binder was precisely sprayed in proper places to be effectively activated using a nozzle operated using a positive displacement valve.

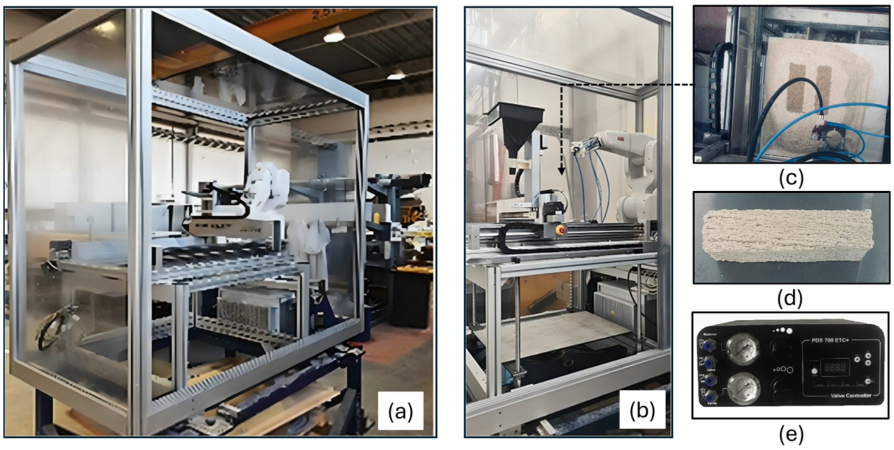

Figure 2. (**a**,**b**) Customized 3D printer setup; (**c**) printed green specimen; (**d**) printed specimen; (**e**) 700 ETC+ valve controller.

The printed samples had dimensions of 160 mm × 40 mm × 40 mm and were produced with a layer thickness of 4 mm and a hatch distance of 4 mm. The velocity of the powder spread was 700 mm/min and the liquid binder was also operated at the same velocity, while maintaining the pressure at 2–4 bar using a 700 ETC+ valve controller (Poly Dispensing Systems, Orgeval, France).

The dry mix included limestone (BETOCARB P2-MX from (Omya SAS, Orgon, France) containing 98.4% calcite)—density 2700 kg/m^3—and standardized sand—density 2640 kg/m^3—(per EN 196-1 [21]) at a ratio of 1:3.

The particle size distribution of limestone and standardized sand was analyzed using the laser scattering technique (Partica LA-960V2—Horiba Scientific, 91120 Palaiseau, France) (Figure 3), and the distributions agreed with the technical data provided by the suppliers.

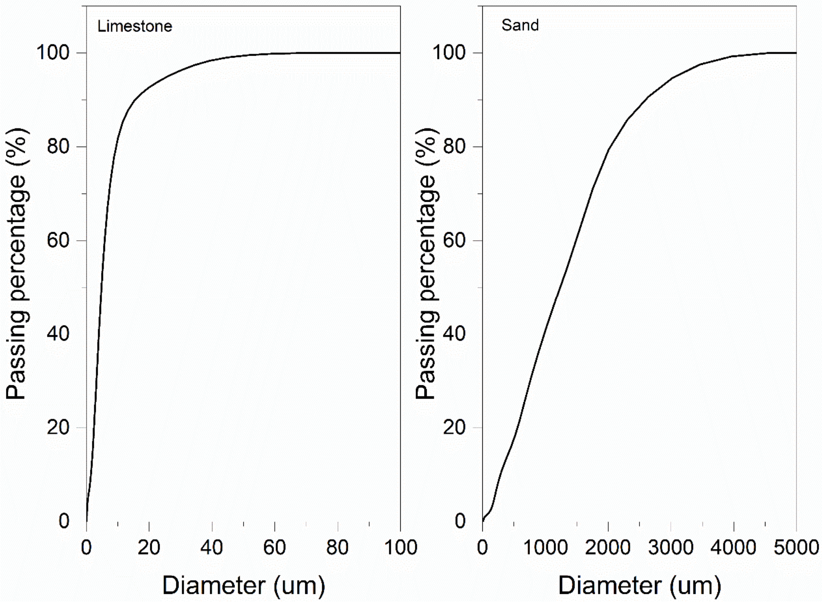

Figure 3. Particle size distribution for limestone and sand.

Three different concentrations of NaOH in water solutions (12.9 mol/L, 15.6 mol/L, and 19 mol/L) were considered in the present work. It is interesting to note that traditional casting techniques have generally utilized around 13 mol/L; however, by utilizing a selective limestone activation process, we were able to safely investigate higher concentrations [20]. The solutions were prepared in an airtight polypropylene Erlenmeyer flask to minimize CO_2 exposure and prevent carbonate formation, and were stored under a controlled hood, along with the other materials, at 20 °C for at least 24 h. The properties of the liquid binders were analyzed using the Anton Paar rheometer MCR 102 in accordance with DIN 53019 [22]; the relationship between shear stress and shear strain is shown in Figure 4.

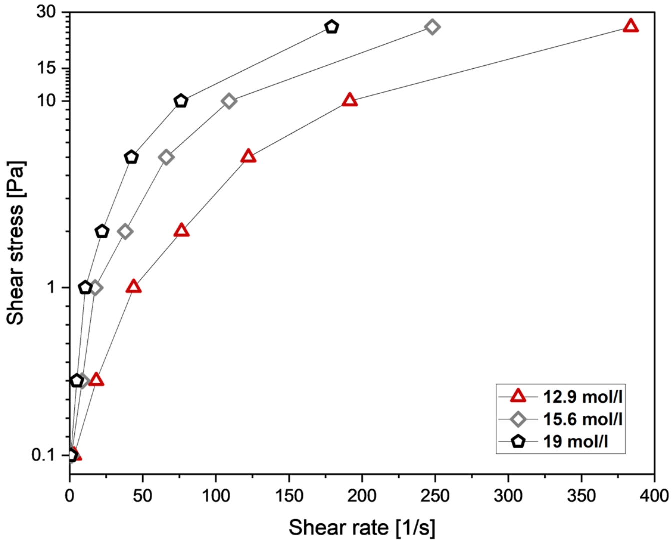

Figure 4. Rheological behavior of the NaOH water solutions.

Printing was carried out by depositing successive 4 mm thick layers (ten) of a mixture of dry limestone and normalized sand, each activated using a NaOH water solution over a defined area of 160 mm × 40 mm. The printed samples were first cured in situ on the powder bed for 24 h to enable the binder to initiate the hydration process and allow for setting without interference. This was followed by additional curing for 48 h at room temperature to enable continued hydration and strength development under air exposure. After curing, loose powder was removed (de-powdering). After printing, the specimens were manually abraded using standardized grit paper in order to achieve reproducible edge profiles that are required for mechanical testing. To ensure a reproducible flat surface, smoothing was conducted on a precision-ground, level steel plate as an invariant reference by maintaining a combination of calibrated hand pressure techniques and continuous visual inspection—and the specimens were intermittently rotated to minimize localized surface deviations. The printed specimens were finally dried at 45 °C for 96 h and 600 h before mechanical testing, which was equivalent to 7 days and 28 days of curing time, respectively. The choice of this drying temperature was based on previous literature [23].

The weight loss of the printed specimens was measured after post-processing to the end of curing time (28 days).

The flexural strength of the cured specimens was measured by three-point bending at curing times of 7 and 28 days, as per norm EN-196-1 [21], using a 3R Quantech, Quantech analyzer (3R—Recherches & Réalisations Rémy, Montauban, France) apparatus with a loading rate of 50 N/s and a span of 100 mm. The resulting values were the mean of three individual values.

The porosity of the printed specimens was measured using Archimedes' method, using portions of the specimens obtained from the mechanical tests. Ethanol was used instead of water to avoid possible dissolution. These measurements were performed 1 to 2 days after the mechanical tests.

The 3D-printed specimens were examined by scanning electron microscopy (SEM, I-Mat, CY Cergy Paris Université, Cergy, France). The microstructure of fracture surfaces (collected from samples used in the mechanical tests) was observed using a Gemini 300 microscope (ZEISS) Jena, Germany in high vacuum mode with a voltage of 2 kV and a working distance of 7.5 mm. In addition to SEM, EDX analysis was performed on different areas of the printed specimen. Sodium and calcium quantification was obtained by the PB-ZAF method.

XRD analysis was carried out with a D8 Advanced instrument (Bruker Corporation, Karlsruhe, Germany) with a copper anode ($(K\alpha) = 1.5406$ Å). Scans were run with a step of 0.0167° and a counting time of 0.5715 s/step from $2\theta = 10°$ to $2\theta = 90°$.

Differential thermal analysis and thermogravimetric analysis (DTA-TGA) were carried out with an STA 449 F1 Jupiter analyzer (Netzsch-Gerätebau GmbH, Selb, Germany,) from 25 °C to 1000 °C with a heating rate of 10 °C/min under a nitrogen flux (50 mL/min). All of the tests were performed using approximately 110 mg of powder.

3. Results and Discussion

3.1. Weight Loss After Printing

The weight loss results are shown in Figure 5 as a function of NaOH concentration up to 28 days of aging. A very fast loss occurs during the first two days, most likely caused by moisture evaporation and initial curing reactions. The 19 mol/L NaOH sample shows the least weight loss and levels off at around −5.5%, while the values for the 15.6 mol/l and 12.9 mol/L specimens level off at around −6.7% and −8.2%, respectively. A similar trend was observed in previous literature [23]. By increasing the NaOH concentrations, the water quantity decreases, and so does the weight loss, as the weight loss is due to the evaporation of the free water that is not required for the curing process. Previous literature also confirms that free water may contribute to the partial dissolution of reaction products and the development of internal stresses [18]. Drying is compulsory to eliminate free water and to improve the mechanical strength. However, rapid drying at higher temperatures results in a decrease in strength, possibly due to the development of stabilizing phases which better resist further dehydration [20,23]. All of the samples evidence that, after 10 days, there is a minimal change in weight, meaning that most of the reactions and drying processes stabilized by then. Overall, a larger NaOH concentration appears to enhance the stability of the samples over time.

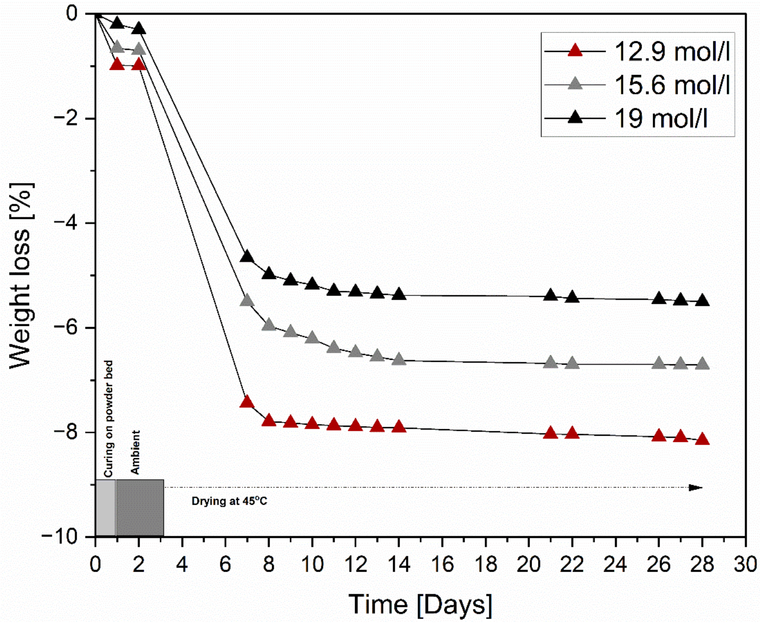

Figure 5. Weight loss of printed samples after printing (24 h curing on the powder bed, 48 h curing at ambient conditions and then drying at 45 °C).

3.2. Identification of the Reaction Product

The XRD spectra of the 3D-printed specimens are shown in Figure 6.

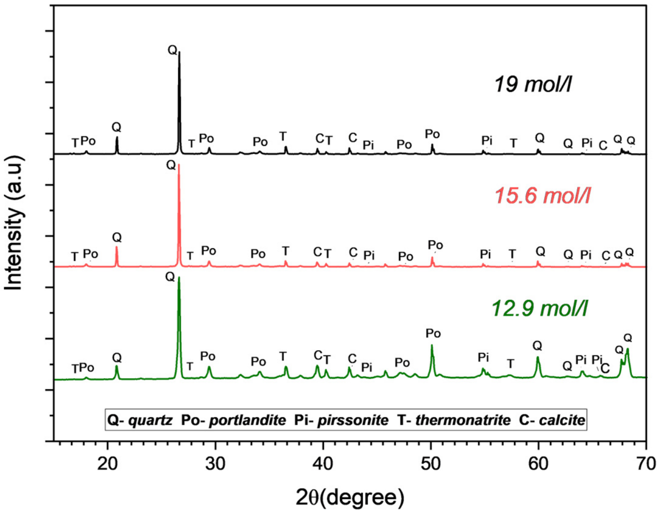

Figure 6. XRD analysis patterns and identified crystalline phases.

All of the XRD patterns show the peaks of quartz related to the presence of standardized sand and calcite from unreacted limestone in the 3D-printed samples. Irrespective of the NaOH molarity, the reaction products are thermonatrite (Na_2CO_3, H_2O), portlandite ($Ca(OH)_2$), and pirssonite ($Na_2Ca(CO_3)_2$, $2H_2O$). Moreover, calcite peaks are visible. They could be associated with unreacted limestone.

TGA−DTA diagrams of samples printed with different NaOH water solutions are shown in Figure 7. They present five endothermic peaks with weight loss and two endothermic peaks without weight loss. Below 200 °C, the observed peaks were attributed to dissociation reaction (water release) in thermonatrite (around 112 °C) and pirssonite (around 170 °C) [24] according to the following reactions, respectively.

$$Na_2CO_3, H_2O \rightarrow Na_2CO_3 + H_2O \tag{1}$$

$$Na_2Ca(CO_3)_2, 2H_2O \rightarrow Na_2Ca(CO_3)_2 + 2H_2O \tag{2}$$

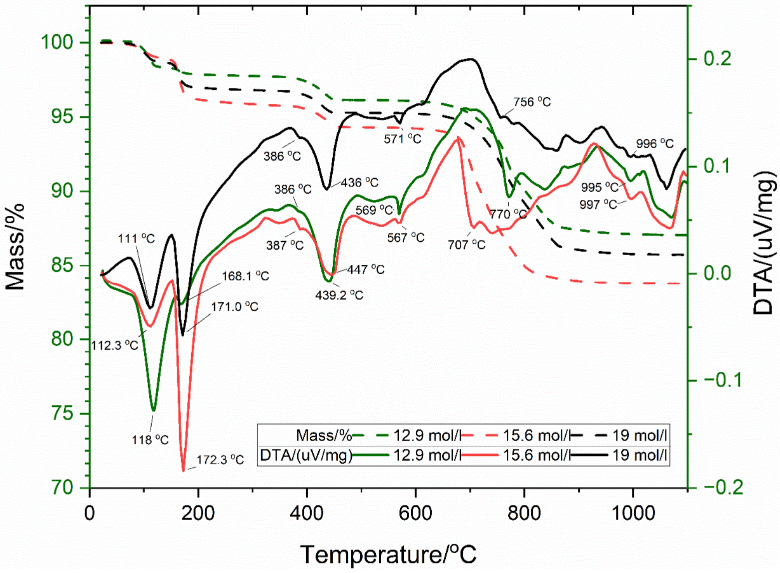

Figure 7. TGA/DTA analysis diagrams.

The peak around 440 °C was related to the dehydration of portlandite (Equation (3)) and was consistent with the literature [25].

$$Ca(OH)_2 \rightarrow CaO + H_2O \tag{3}$$

Above 600 °C, the peaks were linked to the decarbonisation of calcareous compounds: according to previous literature [24], nyerereite ($Na_2Ca(CO_3)_2$ from dehydration of pirssonite) and limestone, according to the following reactions.

$$Na_2Ca(CO_3)_2 \rightarrow Na_2CO_3 + CaO + CO_2 \tag{4}$$

$$CaCO_3 \rightarrow CaO + CO_2 \tag{5}$$

The peaks without weight loss, at 386 °C and around 568 °C, were associated with crystallographic transformations in the nyerereite structure (low-temperature form to high-temperature form) [26] resulting from dehydration of pirssonite and to allotropic transformation of quartz ($\alpha \leftrightarrow \beta$), reported previously [27].

The identified compounds (i.e., thermonatrite, pirssonite, portlandite, calcite, and quartz) were previously identified through XRD analysis. This indicates that all the reaction products were crystallized, whatever the NaOH concentration. The main differences between samples came from the TGA curves and, so, from the quantities of reaction products. Table 1 summarizes all the weight loss measured on TGA curves and the final weight loss after curing (i.e., free water evaporation).

Table 1. Weight loss and water balance of prismatic specimens under different concentrations of NaOH.

NaOH Molarity (mol/l)		**12.9**	**15.6**	**19.0**
Related products and temperature range (°C)	**Thermonatrite (25–140)**	1.8	1.1	1.3
	Pirssonite (140–335)	0.6	3.1	1.9
	Portlandite (335–560)	1.6	1.5	1.5
	Carbonated phases (560–1100)	9.1	10.5	9.5
Weight loss from curing (%)		8.2	6.7	5.5
Total water (%)		12.2	12.4	10.2

The amount of portlandite appears to remain stable, regardless of the NaOH solution's molarity, while the amount of the other reaction products varies with the molarity.

3.3. SEM Analysis

SEM images of the printed specimen with the different NaOH solutions are shown in Figure 8.

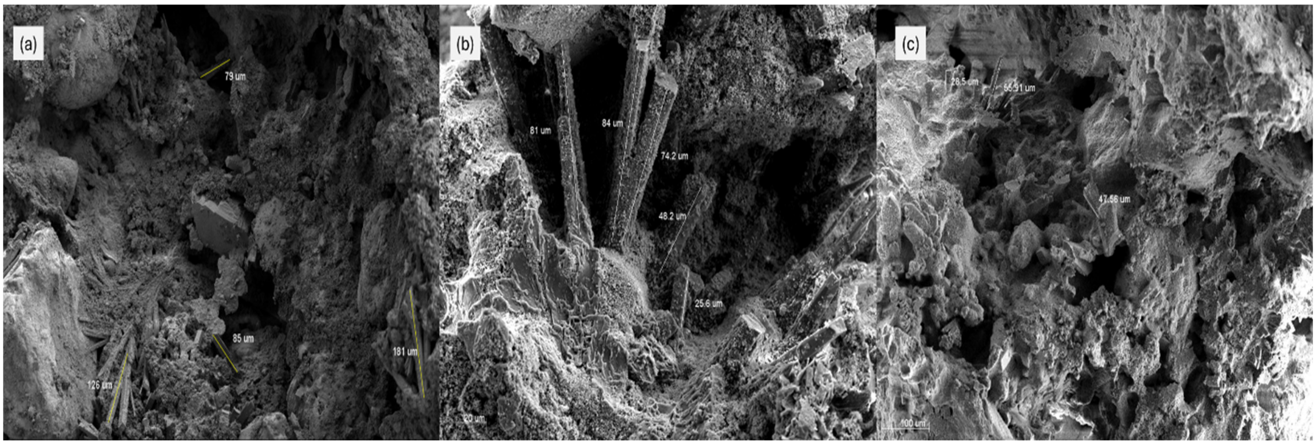

Figure 8. SEM images of the 3D printed sample with different NaOH concentrations: (**a**) 12.9 mol/L; (**b**) 15.6 mol/L; and (**c**) 19 mol/L.

Different microstructures were observed, regardless of the NaOH concentrations used, including dense areas, grainy areas, and needles of different lengths. These microstructures were associated with the compounds identified by XRD and thermal analysis (i.e., thermonatrite, pirssonite, portlandite, and calcite—Figures 7 and 8). To link a microstructure to a compound, a point-counting procedure was conducted. EDX analysis was performed in selected areas, identifying and quantifying the elements present. The quantification was conducted in atomic percentages using the standardless PB-ZAF method in EDX software (https://edx.com/, accessed on 16 April 2025). Then, the Na:Ca ratios were calculated and compared to the theoretical ratios of the identified compounds. They were: 1.15 for pirssonite and 0.00 for calcite and/or portlandite. Figure 9 shows the selected areas for the EDX analysis.

The Na:Ca ratios were 0.1, 1.6, 2.3, and 3.1 for areas I, II, III, and IV, respectively. The shape and the Na:Ca ratio of area I were very close to the shape and values reported in the literature [20], which confirms unreacted or partially reacted calcite. The shape of areas II and IV were similar, but their Na:Ca ratio is different. This suggests that their degree of crystallization might be different or that these crystals may have different natures. They could be related to pirssonite and/or thermonatrite. Area III presents a different shape and an intermediate Na:Ca ratio, indicating a possible mix of the reaction products (i.e., portlandite, pirssonite, and thermonatrite). These microstructural differences are important because they can affect the overall performance of the material. For instance, areas containing unreacted calcite could result in localized weak areas that are detrimental to mechanical strength, while mixed reaction product regions could be a sign of continued hydration or phase stability variations. Heterogeneity in this way could affect durability through its influence on the material's response to environmental conditions, such as moisture or carbonation.

Different microstructures were observed, regardless of the NaOH concentration used, including dense areas, grainy areas, and needles of different lengths.

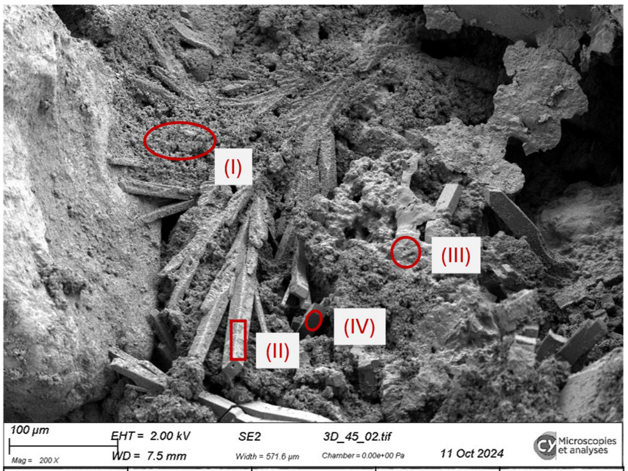

Points	I	II	III	IV
Na/Ca	0.1	1.6	2.3	3.1

Figure 9. SEM−EDX analysis of sample printed with 12.9 mol/L NaOH concentration.

3.4. Porosity

The porosity and the density of the printed specimens are shown in Table 2.

Table 2. Density and porosity of the 3D-printed specimens.

Concentration mol/L	Density (g/cm^3)	Porosity (%)
12.9	1.6 ± 0.2	33 ± 1
15.6	1.6 ± 0.1	32 ± 2
19	1.8 ± 0.1	30 ± 4

The total porosity and density of the specimens was about 31% and 1.7 g/cm^3, respectively, regardless of the concentration of NaOH. The porosity value was larger and the density was slightly smaller than that found in conventional mortar after 28 days (18% and 2.0 g/cm^3) [20]. This important difference very likely depends on the method used for preparing the material and the different water-to-binder ratios used in 3D printing, but the higher water content results in more free water to evaporate during curing [28].

3.5. Mechanical Properties

Flexural strength at 7 and 28 days is presented in Figure 10.

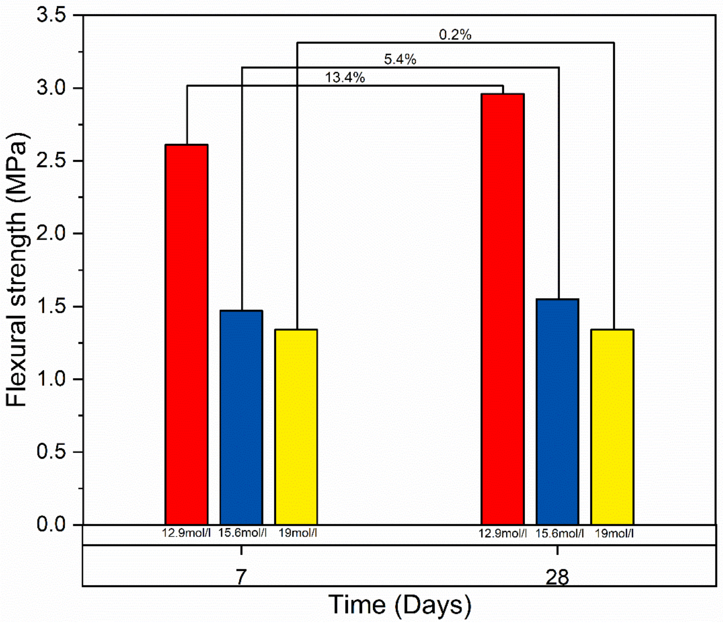

Figure 10. Flexural strength vs. curing time; the strength increase between 7 and 28 curing days is shown.

The results suggest that flexural strength varies with NaOH concentration and curing time. Higher NaOH concentration results in a lower flexural strength. The samples printed with a 12.9 mol/L NaOH concentration show an increased flexural strength by 13.4% from 7 to 28 days of curing. The results of flexural strength can be related to the penetration dynamics of the NaOH solution, which in turn is dependent on its rheological properties. The rheological behavior of a solution, including its properties of flow and viscosity, makes it more challenging to penetrate directly into a powder bed, as represented by the equation derived from Hagen–Poiseuille's law [29]:

$$v = \frac{d(l)}{d(t)} = \frac{r\ \gamma cos\varphi}{4\ \mu\ l(t)} \tag{6}$$

where v is the penetration velocity, l penetration length, r is the pore radius, γ the surface tension of the air–liquid interface, φ the contact angle between the solid and liquid particles, μ the dynamic viscosity of the liquid, and t is the time.

Equation (6) suggests that the penetration velocity v is inversely proportional to the length $l(t)$ and the solution's viscosity. From Figure 3, it is obvious that the 12.9 mol/L NaOH solution has the lowest slope, which means the lowest viscosity. Low viscosity is desirable for penetration into the powder bed as it can flow into fine pores and capillaries easily.

The gain in strength is minimal when the results of printed samples cured after 7 and 28 days are compared. This suggests that the mechanical properties are influenced by the NaOH concentrations, capillary-driven penetration, and curing dynamics. The properties of the printed specimens can be further optimized using these factors.

4. Conclusions

The present work investigates the effects of the concentration of sodium hydroxide water solution on the particle bed bonding during the selective activation of limestone. The results reveal that flexural strength reduces with increasing the NaOH concentration, where the highest strength corresponds to the formulation of 12.9 mol/L—a 13.4% increase from 7 to 28 curing days. This inverse trend emphasizes the need to control alkalinity: while the increased NaOH concentration (e.g., 19 mol/L) increases the initial reaction rates.

Although equal porosity (~31%) and density (~1.7 g/cm^3) are given for every concentration—higher than the traditional mortar standards (18% porosity, 2.0 g/cm^3)—the micro-structural topography is still non-homogeneous. Grainy textures and needle-like crystallites regardless of NaOH concentration are depicted by SEM micrographs. These are the characteristics associated with the crystalline phases identified by XRD analysis, such as thermonatrite, pirssonite, portlandite, calcite, and quartz.

Thermogravimetric analysis (TGA) also helped clarify alkalinity-curing dynamics interactions. Lower NaOH concentrations (12.9 mol/L) exhibited higher weight loss (−8.2%) through extended free water evaporation and geopolymer network consolidation, while the 19 mol/L samples consolidated earlier (−5.5% loss).

These results encourage the understanding of the selective activation of limestone, linking chemistry, microstructure, and processing for scalable 3D printing. Future studies must explore hybrid activators (e.g., mixtures of Na_2SiO_3, and NaOH) or nano clay additives to enhance porosity, accelerate curing, and enhance phase stability at the expense of sacrifice to sustainability.

Author Contributions: M.S.: conceptualization, data curation, formal analysis, investigation, methodology, software, validation, visualization, writing—original draft, writing—review and editing. A.P.: investigation, project administration, resources, supervision, writing—review and editing. A.C.: conceptualization, data curation, formal analysis, investigation, methodology, resources, validation, visualization and writing—review and editing. V.M.S.: funding acquisition, project administration, resources, supervision, visualization and writing—review and editing. All authors have read and agreed to the published version of the manuscript.

Funding: This research was funded by the French National Research Agency (ANR) under the JCJC Project BREATHE (ANR-20-CE22-0001).

Institutional Review Board Statement: Not applicable.

Informed Consent Statement: Not applicable.

Data Availability Statement: The original contributions presented in this study are included in the article. Further inquiries can be directed to the corresponding author.

Acknowledgments: The authors gratefully acknowledge the Università di Trento for covering travel and associated expenses required to carry out this research.

Conflicts of Interest: The authors declare no conflicts of interest.

References

1. Bhushan, B.; Caspers, M. An Overview of Additive Manufacturing (3D Printing) for Microfabrication. *Microsyst. Technol.* **2017**, *23*, 1117–1124. [CrossRef]
2. Doyle, M.; Agarwal, K.; Sealy, W.; Schull, K. Effect of Layer Thickness and Orientation on Mechanical Behavior of Binder Jet Stainless Steel 420 + Bronze Parts. *Procedia Manuf.* **2015**, *1*, 251–262. [CrossRef]
3. Gibson, I.; Rosen, D.W.; Stucker, B. *Additive Manufacturing Technologies: Rapid Prototyping to Direct Digital Manufacturing*; Springer: Berlin/Heidelberg, Germany, 2010; pp. 1–459. [CrossRef]
4. Gibson, I.; Rosen, D.; Stucker, B. *Additive Manufacturing Technologies: 3D Printing, Rapid Prototyping, and Direct Digital Manufacturing*, 2nd ed.; Springer: Berlin/Heidelberg, Germany, 2015; pp. 1–498. [CrossRef]
5. Lowke, D.; Dini, E.; Perrot, A.; Weger, D.; Gehlen, C.; Dillenburger, B. Particle-Bed 3D Printing in Concrete Construction—Possibilities and Challenges. *Cem. Concr. Res.* **2018**, *112*, 50–65. [CrossRef]
6. Pierre, A.; Weger, D.; Perrot, A.; Lowke, D. Penetration of Cement Pastes into Sand Packings during 3D Printing: Analytical and Experimental Study. *Mater. Struct.* **2018**, *51*, 22. [CrossRef]
7. Shakor, P.; Sanjayan, J.; Nazari, A.; Nejadi, S. Modified 3D Printed Powder to Cement-Based Material and Mechanical Properties of Cement Scaffold Used in 3D Printing. *Constr. Build. Mater.* **2017**, *138*, 398–409. [CrossRef]
8. Ingaglio, J.; Fox, J.; Naito, C.J.; Bocchini, P. Material Characteristics of Binder Jet 3D Printed Hydrated CSA Cement with the Addition of Fine Aggregates. *Constr. Build. Mater.* **2019**, *206*, 494–503. [CrossRef]

9. Xia, M.; Nematollahi, B.; Sanjayan, J. Compressive Strength and Dimensional Accuracy of Portland Cement Mortar Made Using Powder-Based 3D Printing for Construction Applications. In Proceedings of the First RILEM International Conference on Concrete and Digital Fabrication—Digital Concrete 2018, Zurich, Switzerland, 10–12 September 2018; Timothy, W., Flatt, R.J., Eds.; Springer International Publishing: Cham, Switzerland, 2019; pp. 245–254.
10. Weger, D.; Lowke, D.; Gehlen, C. 3D Printing of Concrete Structures Using the Selective Binding Method—Effect of Concrete Technology on Contour Precision and Compressive Strength. In Proceedings of the 11th fib International PhD Symposium in Civil Engineering, Tokyo, Japan, 29–31 August 2016.
11. Lowke, D.; Talke, D.; Dressler, I.; Weger, D.; Gehlen, C.; Ostertag, C.; Rael, R. Particle Bed 3D Printing by Selective Cement Activation—Applications, Material and Process Technology. *Cem. Concr. Res.* **2020**, *134*, 106077. [CrossRef]
12. Mai, I.; Lowke, D.; Perrot, A. Fluid Intrusion in Powder Beds for Selective Cement Activation—An Experimental and Analytical Study. *Cem. Concr. Res.* **2022**, *156*, 106771. [CrossRef]
13. Shahid, M.; Sglavo, V.M. Binder Jetting 3D Printing of Binary Cement—Siliceous Sand Mixture. *Materials* **2024**, *17*, 1514. [CrossRef]
14. Salari, F.; Bosetti, P.; Sglavo, V.M. Binder Jetting 3D Printing of Magnesium Oxychloride Cement-Based Materials: Parametric Analysis of Manufacturing Factors. *J. Manuf. Mater. Process.* **2022**, *6*, 86. [CrossRef]
15. Ur Rehman, A.; Sglavo, V.M. 3D Printing of Geopolymer-Based Concrete for Building Applications. *Rapid Prototyp. J.* **2020**, *26*, 1783–1788. [CrossRef]
16. Pichat, P. Fabrication d' Un Matériau Solide à Partir d' Un Hydroxyde Alcalin. WO2006087484A3, 24 August 2006.
17. van Leeuwen, R.; Kim, Y.-J.; Sriraman, V. The Effects of Limestone Powder Particle Size on the Mechanical Properties and the Life Cycle Assessment of Concrete. *J. Civ. Eng. Res.* **2016**, *6*, 104–113. [CrossRef]
18. Ortega-Zavala, D.E.; Santana-Carrillo, J.L.; Burciaga-Díaz, O.; Escalante-García, J.I. An Initial Study on Alkali Activated Limestone Binders. *Cem. Concr. Res.* **2019**, *120*, 267–278. [CrossRef]
19. Avila-López, U.; Almanza-Robles, J.M.; Escalante-García, J.I. Investigation of Novel Waste Glass and Limestone Binders Using Statistical Methods. *Constr. Build. Mater.* **2015**, *82*, 296–303. [CrossRef]
20. Cousture, A.; Renault, N.; Ndiaye, K.; Gallias, J.L. Mechanisms of Alkali-Activation of Limestone: Reaction Kinetics and Influence of Drying Parameters. *Constr. Build. Mater.* **2024**, *441*, 137501. [CrossRef]
21. *EN 196-1:2016*; Methods of Testing Cement—Part 1: Determination of Strength. French Association for Standardization: Paris, France, 2016. Available online: https://standards.iteh.ai/catalog/standards/cen/37b8816e-4085-4dcc-a642-a383d9bddd6c/en-196-1-2016 (accessed on 18 June 2024).
22. DIN 53019. Available online: https://www.austrian-standards.at/en/shop/din-53019-1-1980-05~p3018442 (accessed on 14 April 2025).
23. Cousture, A.; Renault, N.; Gallias, J.-L.; Ndiaye, K. Study of a Binder Based on Alkaline Activated Limestone. *Constr. Build. Mater.* **2021**, *311*, 125323. [CrossRef]
24. Bottcher, M.E.; Gehlken, P.L. Dehydration of Natural Gaylussite (Na2Ca (CO3)(2) Center Dot 5H (2) O) and Pirssonite (Na2Ca (CO3)(2) Center Dot 2H (2) O) as Illustrated by FTIR Spectroscopy. *Neues Jahrb. Fur Mineral. Monatshefte* **1996**, *2*, 73–91.
25. Menéndez, E.; Andrade, C.; Vega, L. Study of Dehydration and Rehydration Processes of Portlandite in Mature and Young Cement Pastes. *J. Therm. Anal. Calorim.* **2012**, *110*, 443–450. [CrossRef]
26. Zucchini, A.; Gavryushkin, P.N.; Golovin, A.V.; Bolotina, N.B.; Stabile, P.; Carroll, M.R.; Comodi, P.; Frondini, F.; Morgavi, D.; Perugini, D.; et al. Crystal Structure of Nyerereite: A Possible Messenger from the Deep Earth. *Am. Mineral.* **2022**, *107*, 2054–2064. [CrossRef]
27. Raman, C.V.; Nedungadi, T.M.K. The α-β Transformation of Quartz. *Nature* **1940**, *145*, 147. [CrossRef]
28. Zheng, S.; Liu, T.; Jiang, G.; Fang, C.; Qu, B.; Gao, P.; Li, L.; Feng, Y. Effects of Water-to-Cement Ratio on Pore Structure Evolution and Strength Development of Cement Slurry Based on HYMOSTRUC3D and Micro-CT. *Appl. Sci.* **2021**, *11*, 3063. [CrossRef]
29. Poiseuille, J.-L.-M. *Experimental Investigations Upon the Flow of Liquids in Tubes of Very Small Diameter*; Bingham, E.C., Ed.; Lancaster Press Inc.: Lancaster, PA, USA, 1940; Volume 1.